scientific reports

Check for updates

OPEN

A roll attitude determination method based on the jamming energy of GEO satellites and an LSTM neural network

Rundong Li[1,2], Lu Feng[1,2]✉, Peng Wu[1,2], Xiangling Deng[1,2] & Haonan Shi[1,2]

Roll attitude determination is crucial for rotating vehicle attitude determination. As research in these areas continues, numerous attitude determination methods have been introduced. Roll attitude determination methods have played a key role in acquiring vehicle information from the Global Navigation Satellite System (GNSS), which was rapidly developed. However, in existing methodological studies, satellite energy information has not been sufficiently analyzed and utilized. This paper presents a roll attitude determination method based on the jamming energy of geostationary orbit (GEO) satellites and a long short-term memory (LSTM) neural network. In this study, a comprehensive model of the energy and roll angle is presented, and the complex properties and common laws of the actual received GEO satellite energy is analyzed. After real-time roll attitude testing of a rotating vehicle using different methods, the proposed method is found to be superior to the traditional least squares (LS) method, with a 48.97% reduction in the mean self-error and a 48.20% reduction in the mean Hall standardized error for the determined roll angles. The research results show that the proposed LSTM deep learning method is more conducive for restoring the complex energy properties of GEO satellites and further enabling accurate real-time roll attitude determination.

Keywords Roll attitude determination, GEO, Satellite jamming energy, LSTM, GNSS, Deep learning

Determining the attitude of a rotating vehicle is necessary for controlling the vehicle. Attitude is not only an important observation in control systems but also an indispensable key parameter in navigation and positioning. Measuring the attitude of a vehicle requires determining its yaw, pitch, and roll angles[1]. When a rotating vehicle has a high rotation speed (5 revolutions per second (rps)–20 rps)[2,3], the task of attitude measurement becomes particularly difficult. High rotational speed conditions will affect the attitude measurement accuracy, and the accumulated computational errors will lead to different degrees of errors in the calculation results. Therefore, there are greater demands for the attitude measurement of rotating vehicles. Thus, attitude measurement methods using information acquired from vehicles need to be specifically discussed.

The conventional attitude measurement method estimates rotational speed by incorporating a rotation phase tracking loop through the advanced spinning-vehicle navigation (ASVN) component[4]. Recent methods such as the extended Kalman filter (EKF)-assisted[5] and submillisecond pseudorange localization[6] methods have been developed to improve the accuracy of vehicle attitude determination. The wide variety of sensors allows different methods to achieve roll attitude determination. Common sensors include solar azimuth sensors[7,8], image sensors[9], and acceleration sensors[10]. However, most of the abovementioned methods are complex, computationally intensive, and require extreme experimental conditions. Gyroscopes have the advantages of high stability and principle and process simplicity, making them common instruments for determining the roll angle of vehicles[11–13]. However, there is a large cumulative error in the gyroscopically solved angular displacement information of a vehicle's rolling angle[14]. Although the cumulative error can be reduced by improving the applied algorithms[15], there are still large amounts of drift errors and cumulative errors.

The traditional high-precision attitude measurement system mainly involves the inertial navigation system (INS)[16], which can simultaneously output navigation information such as position, velocity, and attitude. An attitude determination method based on inertial sensors needs to add bias and scale factors to ensure accuracy.

[1]College of Electronic Communication and Electrical Engineering, Changsha University, 98 Hongshan Road, Changsha 410022, China. [2]Hunan Province Navigation and Attitude Measurement Integrated Application Engineering Technology Research Center, 98 Hongshan Road, Changsha 410022, China. ✉email: fenglu@ccsu.edu.cn

An error in the relevant parameters during the movement of a vehicle can cause a shift in the solution[17]. The Global Navigation Satellite System (GNSS) provides global users with all-weather, all-time, high-precision positioning, navigation, and timing services. In recent years, GNSS positioning technology has developed rapidly and matured[18], and related research has been gradually applied to the attitude determination of rotating vehicles. For example, Shu et al.[19] used multi-GNSS[20] data for high-speed multiconstellation attitude measurements to improve the accuracy of attitude determination. The development of single-antenna-based carrier phase measurement methods[21] has contributed to further understanding the relative positioning between receiving and transmitting antennas, thus improving the accuracy of attitude measurements.

The application of satellite navigation for vehicle attitude determination is increasingly becoming a research focus, especially in terms of achieving high accuracy and reliability. Global positioning system (GPS) satellite navigation for vehicle attitude determination[22–24] requires more than three GPS receivers. However, some vehicles have a small internal space, the update time of the GPS receivers is too long, and the real-time performance is poor. The construction of the global phase of the BeiDou-3 satellite navigation system (BDS-3) has been completed. Orbits can be divided into medium Earth orbit (MEO) satellites, geosynchronous orbit (GEO) satellites, and inclined geosynchronous orbit (IGSO) satellites. Yang et al.[25] proposed a linear model to account for the conversion of the yaw attitude modes of IGSO and MEO satellites and accurately predict the reverse attitude. Accurate estimation of the yaw attitude can now be achieved by an improved data processing method with BDS, IGSO, and MEO satellite information[26]. However, for the BeiDou GEO, relatively little research has been conducted on vehicle attitude measurements. Current navigation systems can perform more precise orbiting by GEO satellites[27] with high vehicle navigation accuracy[28]. Theoretically, the attitude determination of a vehicle can be achieved by utilizing the properties of GEO satellites. According to the GNSS signal transmission property, the satellite energy amplitude is inevitably subject to different degrees of jamming in terms of receiving energy to determine the attitude information. Only by determining the accurate properties of the satellite energy can the attitude determination of the vehicle be further realized.

With the rise of artificial intelligence (AI), deep learning in artificial neural networks (ANNs)[29] is gradually becoming an important method for information processing[30]. In time series predicting, the evolution of deep learning models has been driven by innovations in sequential dependency modeling[31]. Long Short-Term Memory (LSTM), proposed by Hochreiter and Schmidhuber[32], addressed gradient vanishing in recurrent neural networks (RNNs) through gated mechanisms, establishing a standard for capturing temporal patterns[33]. For the prediction of time series such as satellite energy, LSTM neural networks and their variants are more commonly used. Cho et al. introduced Gated Recurrent Units (GRUs), simplifying LSTM by merging gates to reduce parameters while maintaining performance[34]. Bidirectional LSTM (BiLSTM), an extension by Graves and Schmidhuber, enhanced context awareness by processing sequences bidirectionally, proving effective in tasks requiring full temporal context[35]. Bai et al. redefined convolutional approaches with Temporal Convolutional Networks (TCNs), utilizing causal and dilated convolutions for efficient long-range dependency modeling[36]. The Transformer architecture, developed by Vaswani et al., revolutionized the field via self-attention mechanisms, enabling global temporal relationship modeling[37]. These methods have inspired the treatment of jammed energy. To this end, this paper presents a roll attitude determination method based on the jamming energy of GEO satellites with an LSTM neural network. The properties of the actual satellite energy can be learned by the LSTM network, which outputs the network model to predict the future jamming energy and determine the roll attitude in real time.

The contributions of this study are as follows:

(1) Energy and roll angle models are proposed, and their specific correlations are analyzed. The properties of GEO satellites and their prominent role in roll angle determination are sufficiently analyzed.
(2) A new method for determining the vehicle attitude using the received satellite energy is proposed. This method is capable of real-time anti-jamming processing of the satellite energy and determining the real-time roll attitude of the rotating vehicle by combining the energy properties.
(3) This study innovatively combines satellite energy with deep learning methods and uses them for satellite energy processing and rotation vehicle roll attitude determination. Due to the excellent nonlinear mapping ability and self-learning capability of LSTM, the problem of jamming energy, which is difficult to utilize, can be addressed. The real-time anti-jamming prediction of the energy and roll attitude of any GEO satellite at the same rotational speed can be achieved by simply training any set of long-term continuous GEO satellite energy.
(4) By designing a reliable processing strategy with sufficient data acquisition and test verification and relying on reasonable evaluation criteria, it is proven that the LSTM method is more suitable for energy property extraction of jamming satellites and real-time roll attitude determination of the vehicle. It is proven that the method proposed in this paper has certain advantages, universality, and robustness.

The next section focuses on the principle of antenna reception, with descriptions of the correlation model of the GNSS satellite energy and rolling angle and the characteristics of GEO in the use of satellite energy. The third section mainly introduces LSTM neural network methods and the proposed design and presents a treatment strategy for satellite energy. The fourth section introduces the attitude determination method based on the LSTM neural network. By using the energy properties and rolling attitude determination principle mentioned in the previous sections, an attitude determination program is designed in conjunction with the proposed method, and the evaluation indicators of the method are introduced. The fifth section focuses on the experimental programs and an analysis of the results. The focus in this section is on the accuracy of the energy prediction performance and the determination of the rolling attitude achieved by different methods. In the discussion in

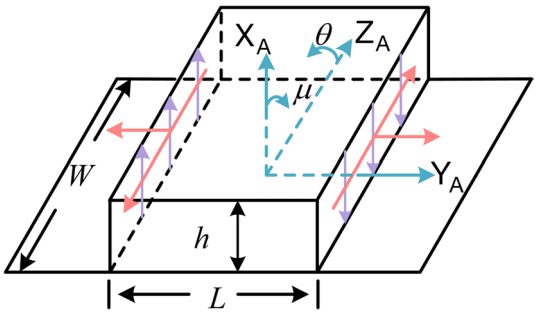

Fig. 1. RMPA structure.

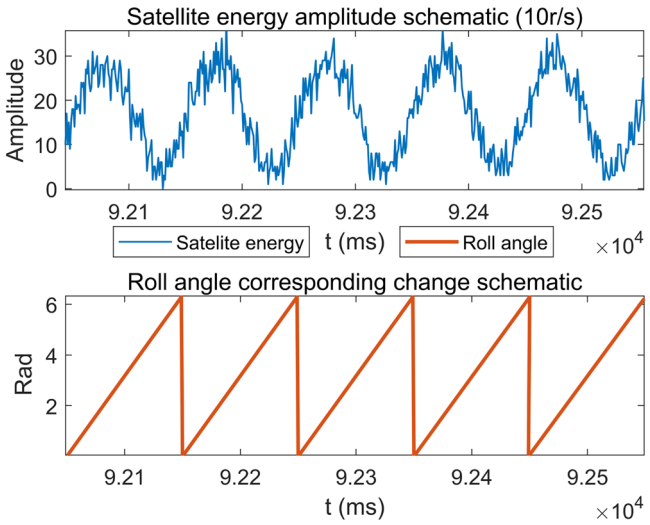

Fig. 2. Schematic of the association between the signal energy and vehicle roll angle.

the sixth section, the impact of non-GEO satellite energies is analyzed, and future solutions are given, followed by perspectives on other attitude determination approaches. Finally, a conclusion of the research is presented.

Establishment of the GNSS satellite energy and roll angle model and analysis of GEO effects

Antenna theory and the definition of the rotating coordinate system

A satellite's energy is received through an antenna. The rectangular microstrip patch antenna (RMPA) on the receiver is analyzed via a transmission line model (TLM), as shown in Fig. 1.

The microstrip sheet of the antenna and the grounding sheet form a section of the microstrip transmission line, and the transmission direction of the quasi-transverse electromagnetic (TEM) wave is determined at the feed point. The two open ends of the transmission line are equivalent to two radiation slits with length W and height h. The slit aperture field is the field strength at the open end of the transmission line. The binary array spacing (effective length) of the two radiation slits is L_e. To utilize the amplitude property of the satellite energy received by the RPMA for roll angle estimation, it is necessary to establish a correlation change model between the energy amplitude of the GNSS signal received by the rolled vehicle and the roll angle of the vehicle. As shown in Fig. 2, the roll angle of the vehicle and the GNSS satellite energy are correlated in one roll period, and both are periodic time functions. To obtain the analytical equation of the function of the energy amplitude and roll angle, as shown in Fig. 2, in this study, the signal transmission model is analyzed in the rotating coordinate system when the energy amplitude reaches its maximum.

Model research and energy characteristics analysis

To research the roll angle, the first step is to define the coordinate system. The Earth-Centered, Earth-Fixed (ECEF) coordinate system can be converted to the rotating coordinate system of the vehicle using the coordinate transformation matrix, with the satellite vector defined as $s_R^{(n)}(x_R^{(n)}, y_R^{(n)}, z_R^{(n)})$. As shown in Fig. 3, the rotating coordinate system O_R—$X_RY_RZ_R$ is defined with the center of the vehicle roll plane O_R as the coordinate origin, and the antenna coordinate system P—$X_AY_AZ_A$ is defined with the antenna phase center P as the coordinate origin. In the antenna coordinate system, PZ_A and O_RZ_R have the same direction, and the unit vector of this

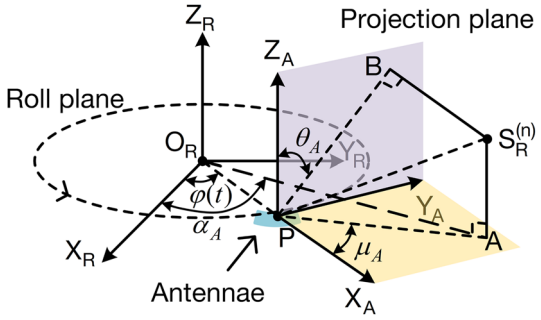

Fig. 3. Schematic of the rotating coordinate system and antenna coordinate system.

direction is $PZ_A = [0, 0, 1]$; the $\mathrm{PX_A}$ direction is the direction indicated by the radius of the antenna phase center; the $\mathrm{PY_A}$ direction is the direction indicated by the tangent line of the P point on the rotation plane counterclockwise; the axis of the $\mathrm{PX_A}$ direction coincides with the extension of the $\mathrm{O_RP}$ line connecting the center of the rotation plane and the antenna phase center; A is the projection of the satellite $S_R^{(n)}$ on the plane YAPXA; A is the projection of the satellite $S_R^{(n)}$ on the plane $\mathrm{Y_APX_A}$; and B is the projection of the satellite $S_R^{(n)}$ on the plane $\mathrm{Y_APZ_A}$.

When the real-time roll angle of the vehicle is set to $\varphi(t)$ and the radius of the roll plane is set to r, the real-time position of the receiving antenna is $P(r \cdot \cos\varphi(t),\ r \cdot \sin\varphi(t),\ 0)$. In the rotating coordinate system, $O_R P$ is in the same direction as PX_A, i.e., $PX_A = [r\cos\varphi(t), r\sin\varphi(t),\ 0]$, and PY_A is orthogonal to PX_A; thus, $PY_A = [-r\sin\varphi(t),\ r\cos\varphi(t),\ 0]$. At this time, the angle of incidence θ_A of the antenna's received signal is the angle between PB and PZ_A, which is shown in Eq. (1). The angle of incidence μ_A is the angle between PA and PX_A, i.e., Eq. 2.

$$\begin{aligned}\theta_A &= 90^\circ - \arccos\left(\frac{PB \cdot PX_A}{|PB|\,|PX_A|}\right) \\ &= 90^\circ - \arccos\left\{\frac{x_R^{(n)}\cos\varphi(t) + y_R^{(n)}\sin\varphi(t) - r}{r\sqrt{\left[x_R^{(n)}\cos\varphi(t) + y_R^{(n)}\sin\varphi(t) - r\right]^2 + \left[z_R^{(n)}\right]^2}}\right\}\end{aligned} \tag{1}$$

$$\begin{aligned}\mu_A &= \arccos\left(\frac{PA \cdot PX_A}{|PA|\,|PX_A|}\right) \\ &= \arccos\left\{\frac{x_R^{(n)}\cos\varphi(t) + y_R^{(n)}\sin\varphi(t) - r}{\sqrt{\left[x_R^{(n)}\right]^2 + \left[y_R^{(n)}\right]^2 - 2x_R^{(n)}r\cos\varphi(t) - 2y_R^{(n)}r\sin\varphi(t) + r^2}}\right\}\end{aligned} \tag{2}$$

According to the RMPA model and the rotating coordinate system, we can further analyze the radiated electric field in the far region of the RMPA, as shown in Eq. 3.

$$\begin{aligned}E_\phi = +j\frac{\beta_A W h E_0 e^{-j\beta_A r}}{\pi r} \cdot \sin\theta_A \cdot \frac{\sin\left(\frac{\beta_A h}{2}\sin\theta_A\cos\mu_A\right)}{\frac{\beta_A h}{2}\sin\theta_A\cos\mu_A} \\ \cdot \frac{\sin\left(\frac{\beta_A W}{2}\cos\theta_A\right)}{\frac{\beta_A W}{2}\cos\theta_A} \cdot \cos\left(\frac{\beta_A L_e}{2}\sin\theta_A\sin\mu_A\right)\end{aligned} \tag{3}$$

where $E_0 = V_0/h$, V_0 is the voltage between the antenna patch and the ground plane, and $\beta_A = 2\pi/\lambda$ is the wavenumber.

When the thickness of the medium is very small, i.e., $\beta_A h \ll 1$, Eq. 4 can be obtained from (3).

$$E_\phi(\theta_A, \mu_A) = \sin\theta_A \cdot \frac{\sin\left(\frac{\beta_A W}{2}\cos\theta_A\right)}{\frac{\beta_A W}{2}\cos\theta_A} \cdot \cos\left(\frac{\beta_A L_e}{2}\sin\theta_A\sin\mu_A\right) \tag{4}$$

According to (4), the approximate waveform properties of the energy can be simulated, as shown in Fig. 4. There is only one obvious peak, and the waveform has a fixed period.

However, unlike the energy model in the ideal case, the actual energy received by the antenna is subject to various kinds of jamming. Modeling the actual energy properties requires specific discussion. In the process of

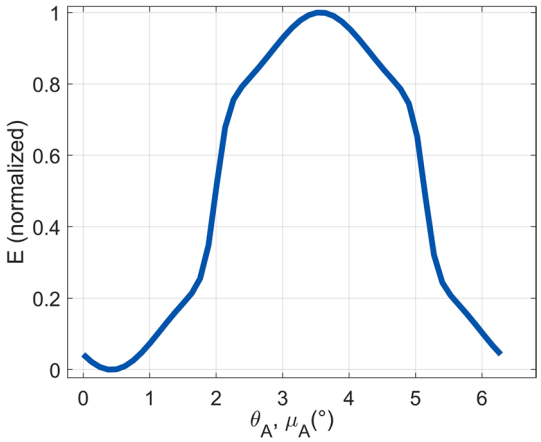

Fig. 4. Simulated example of an ideal energy waveform.

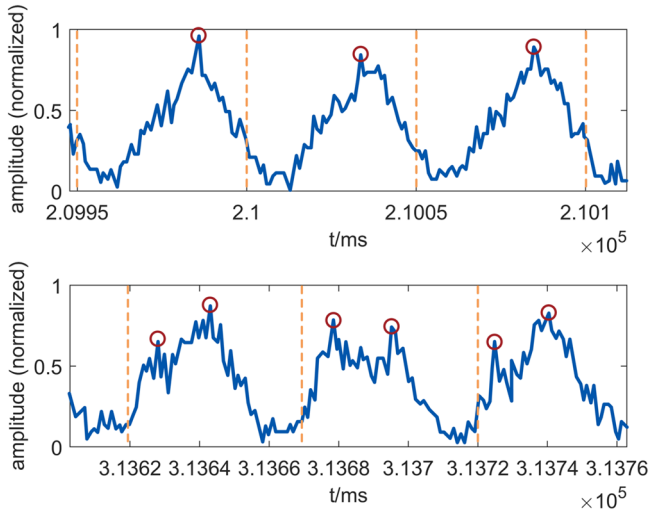

Fig. 5. Schematic of the main energy characteristics of an example (10 rps). The red circles indicate the peak positions, and the yellow dotted lines delineate the period range.

energy emission from the satellite to the antenna, there are two main aspects of jamming: environmental noise and multipath effects[38].

Ambient noise cannot be completely suppressed when rolling energy is harvested. The effect of noise on the energy is usually considered an additive stochastic process. By focusing on the peak properties of the energy, due to the stochastic nature of the noise, the peak position may change. For such cases, a smoothing method or Savitzky–Golay filtering (least squares smoothing filtering) can be applied to achieve different levels of noise reduction[39]. However, such methods may not always correctly reflect the true properties of the energy, and the energy reception situation may be more complex. Satellite signals are reflected by media such as the ionosphere before reaching the receiver, that is multi-path effect. These effects can further lead to frequency-selective fading. Simultaneously, the relative motion between the vehicle and the satellite introduces Doppler shifts. Additionally, multipath and Doppler effects contribute to signal dispersion. All these phenomena must be considered in analyzing their impacts on the actual received energy.

Figure 5 shows a typical example for both cases. As the noise severely affects the amplitude of the energy, the peak energy becomes less stable, i.e., there is some level of error. Therefore, even after applying a smoothing method, the energy peak property is less reliable, making it difficult to restore the exact peak position of the energy. Moreover, the multipath effect alters the overall property of the energy to some extent, and the true peak will be suppressed and jammed by noise. In addition, the peak properties are no longer presented as a single peak but as multiple staggered peaks with regularity. Moreover, these peaks often vary in height, resulting in large errors in the peak positions solved per period.

When affected by these conditions to varying degrees, traditional methods often fail to extract or reduce real energy properties.

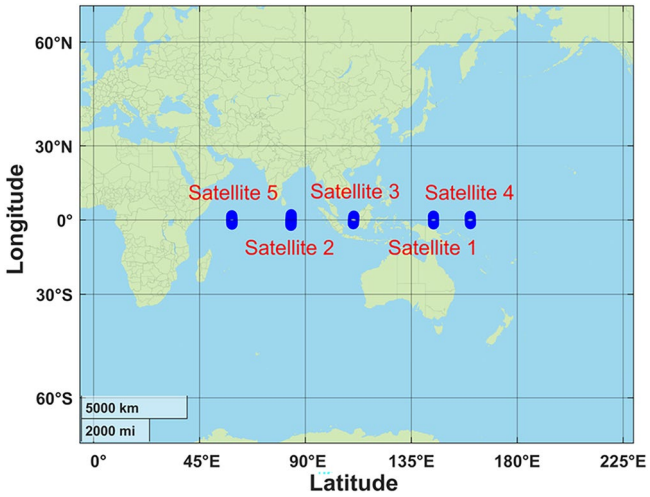

Fig. 6. Twenty-four-hour subsatellite point trajectories (in terms of latitude and longitude) of BeiDou GEO satellites. Satellite trajectory data were obtained by solving receiver ephemeris data. The map images were created by MATLAB R2023b (https://www.mathworks.com/) using the Natural Earth public map dataset (https://www.naturalearthdata.com/).

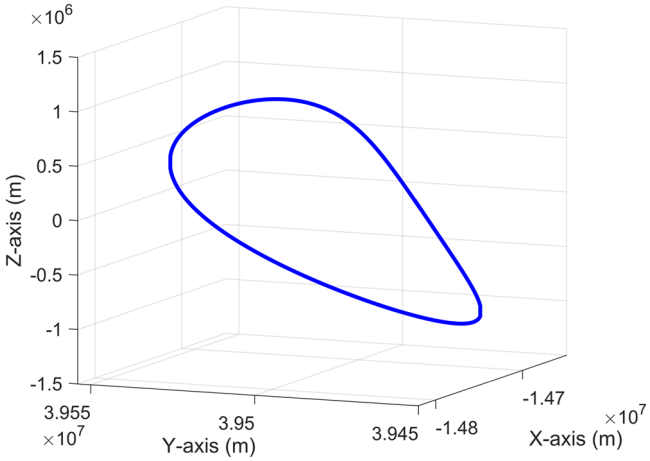

Fig. 7. Twenty-four-hour trajectory of BeiDou GEO satellite #3 (in the ECEF coordinate system).

GEO satellite property analysis for roll attitude determination

According to the correlation model between the GNSS signal energy and the vehicle roll angle, the satellite azimuth angle changes when the real-time coordinates of the satellite change or the receiver position changes significantly. In the BDS, GEO satellites are in a stationary state relative to the ground because their operating angular velocity is the same as the Earth's rotational angular velocity. GEO satellites are located in the visible space of the service area for a long time, their utilization rate is higher than that of other satellites, and the signal strength is more uniform. Figure 6 shows the subsatellite point trajectories of the BeiDou 1–5 GEO satellites drawn according to the received ephemeris after 24 h of continuous observation by receivers.

Figure 7 shows the changes in the coordinates of BeiDou GEO satellite #3 in the ECEF coordinate system according to the received ephemeris after 24 consecutive hours of observation by receiver. As shown in the figure, the changes in the coordinates traversed by the GEO satellite during one operation period are almost negligible. Therefore, the influence of the position change of the GEO satellite in orbit on the azimuth angle can be ignored, and the azimuth angle will only be related to the location of the vehicle receiver.

As shown in Fig. 8, the variation in the direction angle of the GEO satellite is received by the receiver when it is at different positions on the surface and undergoes rolling motion. When a vehicle is in flight, there are usually minimal changes in latitude and longitude between the launch and landing positions. Thus, the azimuth angle of the GEO satellites in the rotating coordinate system remains essentially unchanged during flight. The flight trajectory of sounding rocket-type vehicles typically follows a vertical path into the sky, with minimal coordinate changes. Because of the same latitude and longitude, the azimuth of the GEO satellite in the rotating coordinate system almost does not change. Figure 9 shows that when the vehicle changes along the longitudinal

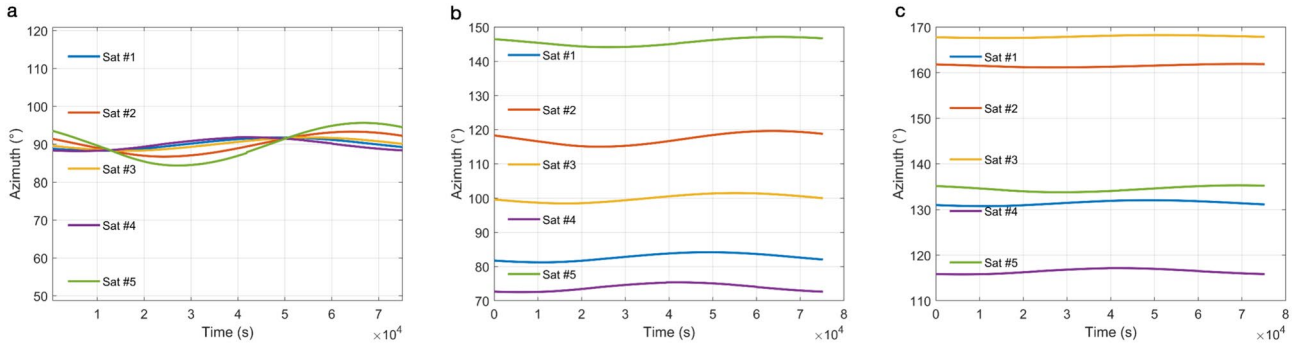

Fig. 8. Variation in the GEO satellite direction angle for different vehicle receiver positions on the ground surface: (**a**) The longitude is 40°, and the latitude is 0°. (**b**) The longitude is 40°, and the latitude is 30°. (**c**) The longitude is 100°, and the latitude is 60°

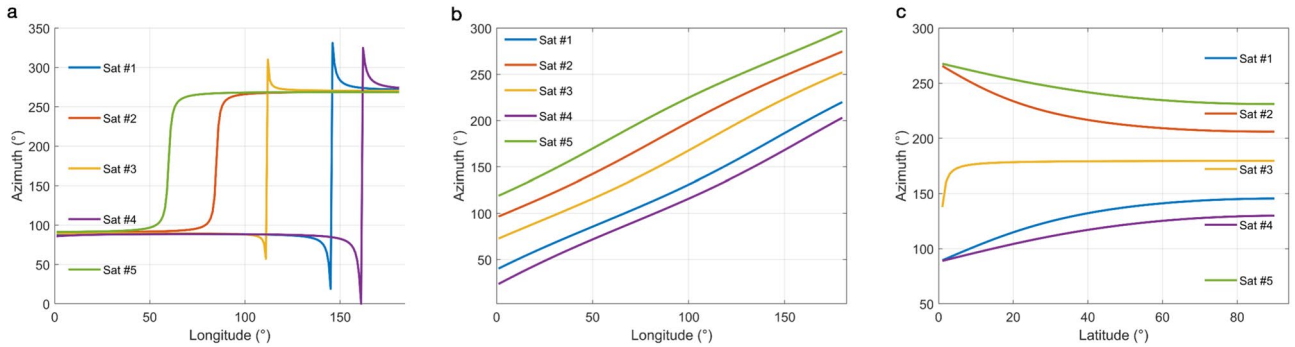

Fig. 9. Changes in the GEO satellite orientation angle as the vehicle receiver moves along the latitudinal and longitudinal lines: (**a**) The latitude is 0° (equator), and the longtitude is changing. (**b**) The latitude is 60°, and the longtitude is changing. (**c**) The longtitude is 110° (same as beidou satellite #3), and the latitude is changing.

and latitudinal directions, respectively, five GEO satellites have the same azimuth on the equator (when passed, reversing 180°, Fig. 9a), and the azimuth changes regularly in other situations (Fig. 9b-c). Combined with the haversine function to calculate the distance change corresponding to the change of latitude and longitude, it is analyzed that when the vehicle moves about 110 km, the direction angle changes by about 0.9°. It suggests that the effect of the azimuth change produced by the firing of the general missile is almost negligible.

From the above analysis, it is noted that the change rule of the energy of the BeiDou GEO satellite signal received when the vehicle undergoes rolling motion is stable, especially at its peak. Therefore, if the GEO satellite signal energy is used for vehicle roll angle detection, empirical data can be utilized to enhance the accuracy of roll angle measurements.

Neural network modeling for energy processing

In this section, the principles of LSTM and satellite energy processing strategies are introduced. Since the energy properties reflected in the actual energy processed by traditional methods cannot be regarded as completely real and deep learning methods have abundant experience in data feature extraction and prediction, deep learning methods are introduced to process satellite energy data. Considering that the energy data are time series and have periodic properties, LSTM can be utilized. And the mainstream time series predicting models BiLSTM, GRU, TCN, and Transformer models can be used as benchmarks. A deep learning method can be introduced, and the results of this method can be analyzed in conjunction with the proposed satellite energy-based roll attitude determination method. After the determination of the processing strategy, relevant indexes are proposed for method performance evaluation and result analysis.

Deep learning model recommendations

LSTM networks are a special type of RNNs. These networks are designed to address the issues of vanishing and exploding gradients that traditional RNNs face when processing long sequences of data. LSTMs manage the flow of information using three gates—a forget gate F_t, an input gate I_t, and an output gate O_t—along with memory cells C_t with the same shape as that of the hidden state H_t, allowing them to efficiently capture long-term dependencies. For the attitude measurement, the attitude changes linearly and continuously over time. These changes can be captured by the LSTM network well. Moreover, the use of the LSTM deep learning algorithm is

more favorable for digging out the roll attitude information, which is contained in the satellite energy signals, and applying it to attitude determination. Figure 10 shows the cellular unit architecture of the LSTM network. In this figure, each line carries a complete vector representing the output from one node to the inputs of other nodes. Each yellow box represents a neural network layer, and the blue circles represents pointwise operations.

The gate inputs for both long- and short-term memories are the current time step input X_t and the previous time step hidden state H_{t-1}. The outputs are computed by applying the sigmoid activation function to the fully connected layer. Assume that the number of hidden cells is h, given inputs $e_t \in \mathbb{R}^{n\times d}$ at time step t and the hidden state $H_{t-1} \in \mathbb{R}^{n\times h}$ at the previous time step. The number of samples is n, and the number of inputs is d. The term e_t contains the properties of the satellite energy over a sufficient period that will be used as input to the LSTM unit cell for continuous network iteration. Candidate memory cells $\tilde{C}_t$ use the $\tanh$ function as the activation function. Mathematically, the LSTM architecture is demonstrated in Eqs. (5)–(10).

$$F_t = \sigma(W_f \cdot [H_{t-1}, e_t] + b_f) \tag{5}$$

$$I_t = \sigma(W_i \cdot [H_{t-1}, e_t] + b_i) \tag{6}$$

$$\tilde{C}_t = \tanh(W_c \cdot [H_{t-1}, e_t] + b_c) \tag{7}$$

$$C_t = F_t * C_{t-1} + I_t * \tilde{C}_t \tag{8}$$

$$O_t = \sigma(W_o \cdot [H_{t-1}, e_t] + b_o) \tag{9}$$

$$H_t = O_t * \tanh(C_t) \tag{10}$$

where W_f, W_i, W_c, and W_o are the weight matrices associated with each gate; b_f, b_i, b_c, and b_o are deviation vectors; $\sigma(x) = 1/(1 + exp(-x))$ is the logistic sigmoid function; $tanh(x) = (e^{2x} - 1)/(e^{2x} + 1)$ is the hyperbolic tangent function; and $*$ represents the Hadamard product operator.

The forget gate layer F_t determines how much of the previous information collected from the combination of H_{t-1} and e_t is affected. If F_t equals 1, the model remembers previous information, whereas if F_t equals 0, the model forgets previous information. In continuous iterative operations, the forget gate layer will maximally preserve the common properties contained in the pure energy signal and forget a certain part of the noise component and multipath fading. The input gate layer I_t selects the satellite energy information to be stored in the unit memory cell C_t and in the candidate memory cell $\tilde{C}_t$. The output gate layer O_t contains the satellite energy information that is filtered and processed through the unitary memory cell C_t. Such an iterative learning process enables better learning of properties that are masked by satellite energy, and thus, more accurate attitude determination can be achieved.

LSTM network design and satellite energy prediction strategy

The architecture shown in Fig. 11 includes an LSTM neural network with an iterative prediction strategy. e_n represents the raw observational data with satellite energy properties as input; e_n^{Train} represents the normalized energy data containing $1 \times t$ time-step sizes after preprocessing, which is used as the training set for the LSTM neural network; e_k^{Test} represents the energy data to be analyzed containing $1 \times k$(k is the size of the data) sizes, which is equivalent to the test set; e_k^{Pred} represents the end of the iterative prediction algorithm; the time to align the test values with the predicted values to obtain the final set to be compared e_T^{Test} and e_P^{Pred}, $T \in [1, k-1], P \in [2, k]$; and $e_P^{Pred'}$ represents the actual predicted value obtained after inverse normalization, which is compared with e_T^{Test} to analyze the performance of the LSTM neural network algorithm. The LSTM layer contains h LSTM cellular units for recursive processing. The dropout layer[40] improves the neural network by reducing overfitting and guaranteeing stable operation of the network architecture. The fully connected layer connects each neuron to all neurons in the previous layer. Each connection has a weight for linear transformation.

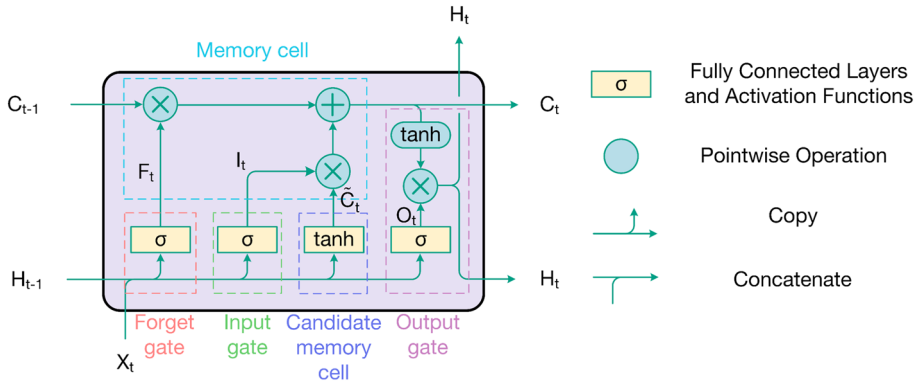

Fig. 10. LSTM cellular unit architecture. This architecture can be divided into 5 parts: the forget gate, input gate, output gate, memory cell, and candidate memory cell, corresponding to the mathematical expressions.

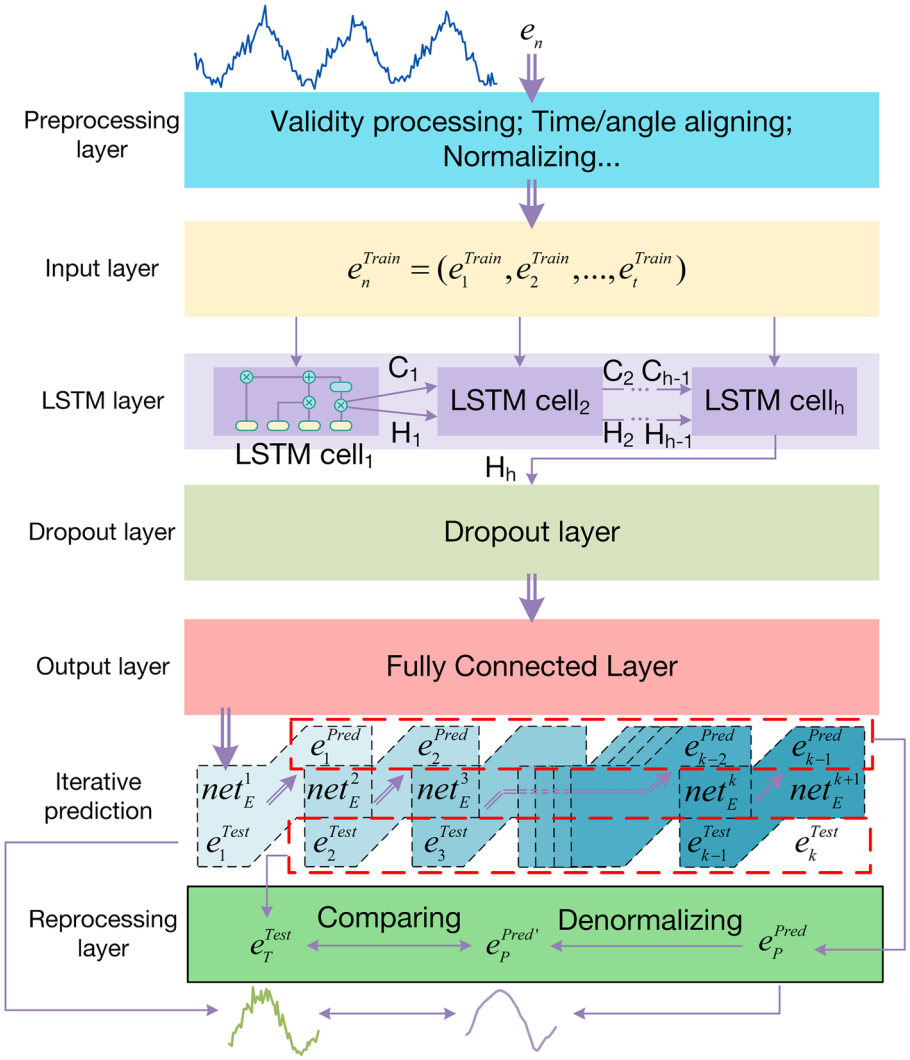

Fig. 11. LSTM network and prediction strategy architecture. This architecture includes an LSTM network with an input layer, an LSTM layer, a dropout layer and an output layer and an energy prediction strategy, which includes a preprocessing layer, an iterative algorithm, and a reprocessing layer.

After the execution of the fully connected layer, the output network net_E^1 variable net is used as the initial network variable for the prediction algorithm.

The preprocessing layer mainly intercepts the available energy data and implements time or angle alignment and normalization for neural network training. In the algorithm, a single-step prediction is implemented, predicting one data point for each input. The network state is updated in real time for each predicted piece of data before proceeding to the next prediction. Finally, the inversely normalized predicted data are compared with the test data to complete the model evaluation and data analysis.

LSTM model parameter design

During model training, network parameter estimation plays an important role in improving the prediction accuracy and efficiency. As shown in Table 1, the LSTM model parameters are optimized using grid search and cross-validation algorithms. The learning rate is a crucial concept in machine learning and deep learning that directly affects the efficiency and final performance of the model training and is a key parameter for achieving model optimization. Gradient descent[41–43] adjusts the learning rate through certain strategies so that the model can converge more fully. From a mathematical point of view, the learning rate is a scalar in gradient descent algorithms that weighs the step size of the objective function (or loss function) descending along the negative gradient direction, i.e., Eq. 12. Assuming that the inputs and outputs of function $J : \mathbb{R} \to \mathbb{R}$ are scalars, and

$$P_{new} \leftarrow P_{old} - \varepsilon \nabla J(P) \tag{11}$$

where P represents the model parameters, ε represents the learning rate, and $J(P)$ represents the gradient of the objective function J relative to P. P_{old} represents the model parameters before gradient descent, and

Number	Parameter	Value
1	Loss function	MSE
2	Metrics	RMSE
3	Optimizer	Adam
4	Max epochs	35
5	Gradient threshold	1
6	Initial learning rate	0.001
7	Learning rate schedule	Piecewise
8	Learning rate drop period	10
9	Learning rate drop factor	0.8
10	Input dimension size	1
11	Output dimension size	1
12	Number of LSTM layers	2
13	Number of hidden units	50
14	Dropout probability	0.3
15	Size of mini batch	32
16	Shuffle	Every-epoch

Table 1. LSTM model training parameter settings.

P_{new} represents the model parameters after gradient descent. The value of the objective function J can be continuously reduced by the gradient descent algorithm.

The adaptive moment estimation (Adam) algorithm is commonly used in regression problems to train networks. This algorithm uses both order moments and second-order moments to adjust the learning rate and obtain the global minimum loss. In this paper, in addition to using the Adam algorithm, the gradient descent algorithm is implemented using a time decay strategy to achieve optimal convergence.

In this strategy, the learning rate decreases with the number of training iterations, as shown in Eq. 13.

$$\varepsilon_t = \varepsilon_0 \times (1 + \gamma \times t)^{-p} \tag{12}$$

where ε_t represents the learning rate of the t th iteration; ε_0 represents the initial learning rate; γ represents the decay factor; and p represents a positive real number to control the rate of decay. The selection of the learning rate parameter was finally determined to have a more appropriate value through repeated experiments and comparison of the effects.

The overall structure uses double-layer LSTM for sufficient energy feature learning. A mini-batch of samples is used for iteration in each round of learning, which significantly increases the computational efficiency. Dropout is added to prevent overfitting[40] and facilitate subsequent uncertainty analyses.

LSTM-based roll attitude determination method

The main methodological flow used in this section is shown in Fig. 12. This flow mainly consists of a method for determining the roll attitude by the satellite energy and an energy processing strategy combined with an LSTM deep learning method.

Energy peak solving roll angle method

After the satellite energy modeling, the principle of energy signal reception, the introduction of the LSTM neural network, and so on, this section will finalize the solution of the roll attitude determination. As shown in Fig. 12b, the local Cartesian coordinate system (or east–north–up (ENU) coordinate system) is constructed to calculate the observation vector and elevation angle of the satellite. The location point O where the user is located is the coordinate origin, and the three coordinate axes are mutually perpendicular east (E), north (N), and up (U).

When analyzing a projection, i.e., Fig. 12a, S_i' is the point where the satellite S is projected to the roll plane, and the satellite azimuth α is the angle at which the N-axis is clockwise to the projection direction of the observation vector in the horizontal plane. The antenna is placed on one side of the vehicle to roll with the vehicle, assuming that the forward direction of the vehicle is the N direction, the direction perpendicular to the antenna is the U direction, and the plane formed by the U' axis and the E axis is defined as the roll plane. The U' axis and E' axis are the coordinate axes that change after rotation. The angle from the E-axis to the projection direction of the observation vector in the roll plane is defined as the roll angle φ.

According to Fig. 12a-c, we focus on the moment when the energy peaks at the point where the vehicle rolls until the antenna is directly in front of the satellite, at which point the roll angle φ coincides with the satellite azimuth angle α corresponds to $\alpha_R^{(n)}$ in Eq. 13. As the vehicle rolls, the energy at each moment corresponds to the antenna position, and the ideal waveform is shown in Fig. 12c. For a determination period, the moment $t_{\max}^{(n)}$ when $e(t)$ peaks is found. Combining this solution with the analysis presented in Sect. 2.2 yields Eq. 13.

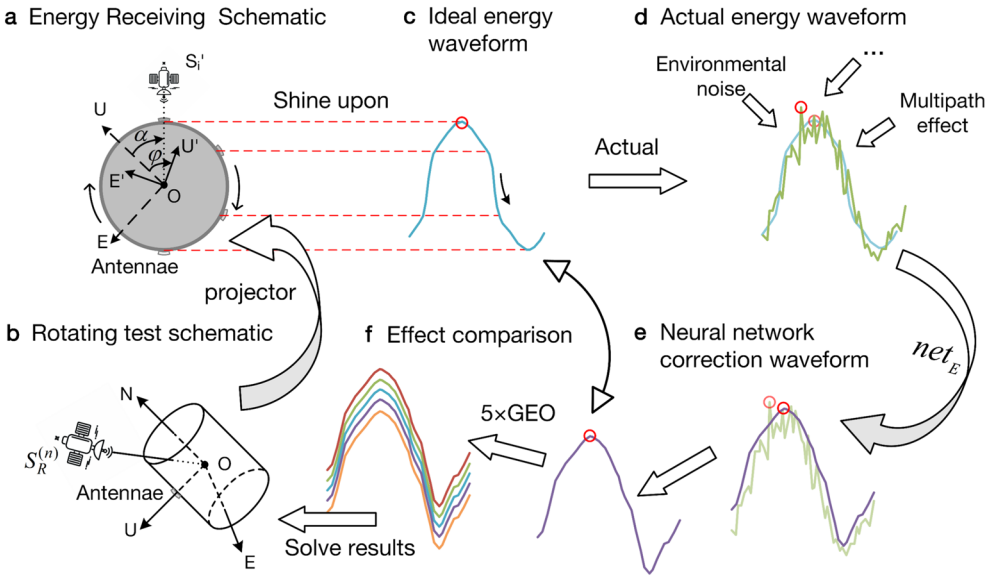

Fig. 12. Overall methodology flow. (**a**) Projection of the N side of a rotating table. The shaded part changes from darker to lighter to represent the change in antenna position. When the sights coincide (OS_i' and OU'), the energy peaks. (**b**) Overall schematic of the roll test with the antenna on the side of the vehicle. (**c**) Red circles indicate the locations of the peaks. (**d**) The actual energy peak feature are masked due to various influences. (**e**) The energy features are extracted by the neural network prediction. (**f**) The network performance can be analyzed by comparisons. After synthesizing results of five GEO satellites, the final more precise results can be solved.

$$\varphi(t_{\max}^{(n)}) = \alpha_R^{(n)} = arctg\left[\frac{y_R^{(n)}}{x_R^{(n)}}\right] \tag{13}$$

If the energy signal sampling rate is f_s and the vehicle rotational speed is f_r, the roll angle at any moment ($t \geq t_{\max}^{(n)}$) can be extrapolated from Eq. (14), as shown in Eq. 14.

$$\varphi(t) = 2\pi f_r(t - t_{\max}^{(n)}) + \alpha_R^{(n)},\ (\mathrm{mod}\ 2\pi) \tag{14}$$

The overall mapping relationship can be expressed as follows: the roll angle at the peak moment of the energy signal is equal to the azimuth angle. Since the azimuth angle of the GEO satellite is known, the roll angle at the peak can be obtained, and the roll angles at all other time points can be extrapolated accordingly.

However, as shown in Fig. 12d, the energy reception in the actual test is inevitably affected by environmental noise, mainly Gaussian white noise, multipath effects, etc. Notably, the noise will affect the properties of the energy waveform to different degrees, resulting in peaks being easily masked and the peak positions exhibiting unstable jitter, thus affecting the determination of the roll angle. The multipath effect will affect the overall property of the energy, and due to inherent effects such as the inhomogeneity of the ionosphere, the waveform of the energy appears to have a special unpredictable multipeak characteristic, and the real peak is completely masked, which cannot be used to determine the roll angle using conventional methods.

In this method, an LSTM neural network is introduced to predict and detect the real energy signal to achieve the effect shown in Fig. 12e. The training involves selecting a portion of the continuous satellite energy with apparent properties from the test that is as long as possible and has low multipath effects as the neural network input. Through the back transmission and forward transmission of the LSTM network, continuous iterations are applied to finally obtain the network state at that rotational speed, and this parameter is used as a control variable. When new satellite energy with the same rotational speed is received, real-time energy anti-jamming prediction and attitude solving can be realized by using the iterative prediction strategy in this paper. Eventually, as shown in Fig. 12f, the theoretical energy properties are compared with the predicted energy to verify the network performance. Finally, the roll angle of the vehicle under a certain satellite can be analyzed by synthesizing five GEO satellites.

Evaluation indexes

To assess the performance of the proposed method in this paper, three evaluation metrics are introduced—the root mean squared error (RMSE), the mean absolute error (MAE), and the mean absolute percentage error (MAPE)—as shown in Eqs. (15)–(17), respectively.

$$RMSE = \sqrt{\frac{1}{k}\sum_{i=1}^{k}(e_i - \hat{e}_i)^2} \tag{15}$$

$$MAE = \frac{1}{k}\sum_{i=1}^{k}|e_i - \hat{e}_i| \tag{16}$$

$$MAPE = \frac{1}{k}\sum_{i=1}^{k}\left|\frac{e_i - \hat{e}_i}{e_i}\right| \times 100 \tag{17}$$

where k represents the total length of the test data, e_i represents the true value, and $\hat{e}_i$ represents the measured value. The MAE is the mean of the sum of the absolute differences between the actual and predicted values, which reflects the closeness of the predicted value to the measured value on an absolute scale. The RMSE scales up and severely penalizes large errors through the use of the squared form. The MAPE is sensitive to the relative error and does not change due to the global scaling of the target variables.

To evaluate the anti-jamming effect of the method for roll angle determination, the standard deviation (*StD*) and $RMSE_{Hall}$ are introduced to assess the stability and accuracy of the roll attitude determination method results, respectively. The value of *StD* represents the degree of stability of the energy-solved roll angle, and a smaller value represents an overall smoother and less floating amplitude, as shown in Eq. 18. Finally, the solved roll angle is compared to the roll angle synchronously output by the Hall sensor, and the $RMSE_{Hall}$ is calculated using the roll angle output by the Hall sensor as the standard, as shown in Eq. 19. A smaller $RMSE_{Hall}$ represents a smaller solution error, which verifies the accuracy of the method for roll attitude determination.

$$StD = \sqrt{\frac{1}{d}\sum_{i=1}^{d}|\varphi_i - \bar{\varphi}|^2} \tag{18}$$

$$RMSE_{Hall} = \sqrt{\frac{1}{d}\sum_{i=1}^{d}(\varphi_i - \varphi_{Hall})^2} \tag{19}$$

where d is the number of roll angle samples solved from the data; $\overline{\varphi}$ is the overall average of φ_i; and φ_{Hall} represents the roll angle output from the Hall sensor in real time.

Experiment and results

This section focuses on the experimental scenario, experimental results, and analysis. First, the experimental platform for the roll test and the energy-receiving scheme for the roll test are introduced. Then, appropriate parameters are selected for model training to obtain a high-performance model. Afterward, the effectiveness and stability of the models and methods are qualitatively evaluated according to the results of the evaluation indexes. Finally, the roll angle derived from different methods is quantitatively compared and analyzed with the roll angle given by Hall sensors at the same moment, verifying the superiority of the method proposed in this paper.

Experimental scenario and program

The experimental scenario is on the roof of a building, and the sky-to-sky test is performed by rotating the vehicle. As shown in Fig. 13, an RPMA is installed on one side of the vehicle to roll with the vehicle. Inside the vehicle, a GNSS receiver is installed to receive satellite energy together with the RPMA and realize transmission and storage. The whole vehicle is on a rotary table, and a programmed motor is installed at the other end of the rotary table. A personal computer (PC) controls the programmed motor to precisely control the rotation angle and speed of the vehicle. Many wave-absorbing materials are placed around the rotary table to minimize the reflection and jamming of the satellite signals and ensure the accuracy of the experimental data. Finally, the data are output to the PC through a serial port for further processing.

In the experimental setup, most signal interference effects are suppressed. Specifically, the receiver employs spread-spectrum technology to enhance signal bandwidth, significantly reducing frequency-selective fading. Wave-absorbing materials mitigate multipath effects. For GEO satellites, the radial velocity relative to the vehicle is approximately zero, and since this study focuses solely on the vehicle's roll attitude, the Doppler shift caused by radial motion within the roll plane is negligible. By accounting for these factors, the phase variations induced by signal propagation delays can be treated as linear, allowing dispersion-induced waveform distortions to be ignored.

To verify the universality and accuracy of the method, the following data reception and method testing scheme is used in this experiment: five GEO satellites from BeiDou-3 are selected, and the satellites are verified. The energy from each of the five GEO satellites is received in parallel and stored in real time. A total of one week of testing is performed. There are three tests each day, i.e., in the morning, midday, and evening. The GEO satellites around the earth are represented in three groups. Each group of tests is divided into 2 rps, 10 rps, and 20 rps, representing low, medium, and high rotational speeds, respectively. The detailed data can be verified by the experiments. In the experiments, a continuous section of data at each rotational speed, where the energy

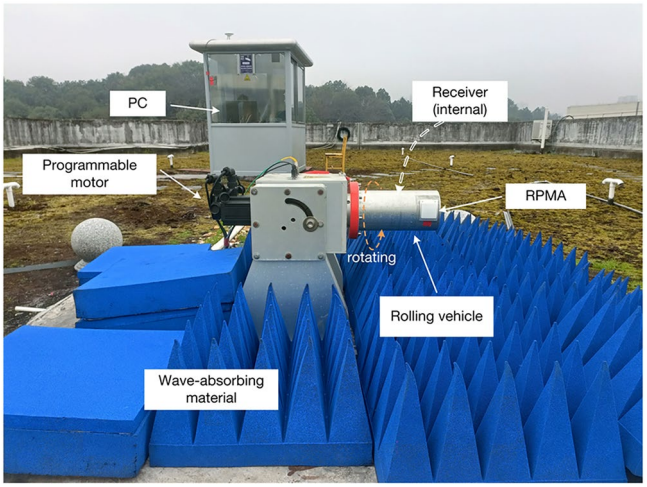

Fig. 13. Roll test energy reception experimental scenario.

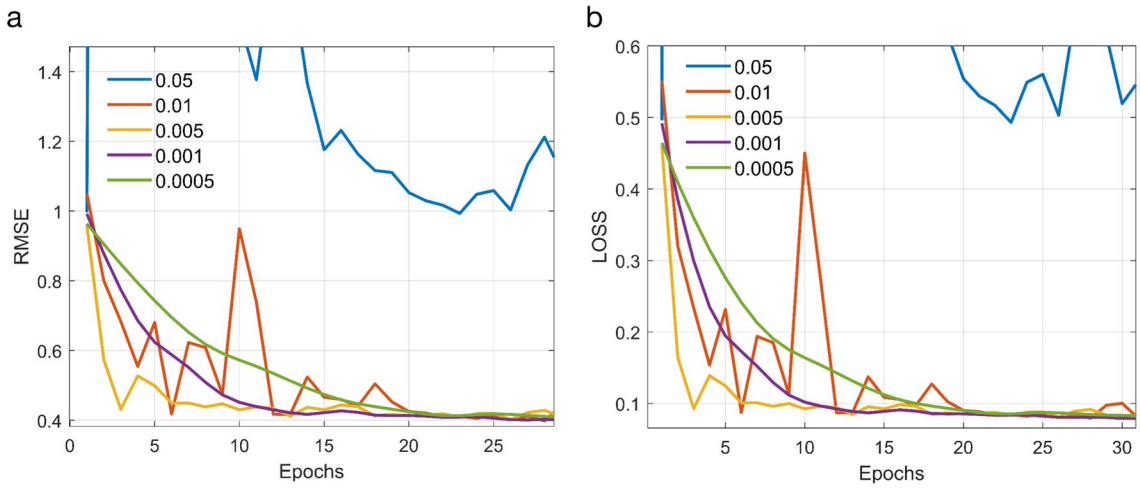

Fig. 14. Model training process diagram: (**a**). RMSE. (**b**). LOSS.

is less affected by multipaths and as continuous as possible, is selected as the training set for the LSTM neural network model. The training is conducted according to the methods and strategies mentioned in Section "Model research and energy characteristics analysis", and finally, real-time tests can be performed for each dataset. The time selection is 10 periods (fixed period time), 20 s (short-term time), and 100 s (long-term time). The models and methods can be evaluated through the statistics of the experimental results.

Test results

The different experimental methods can be preanalyzed by testing typical satellite energy data. The *RMSE* and *LOSS* of the actual training process of the LSTM model are shown in Fig. 14, where LOSS is basic MSE function. Regardless of the *RMSE* or *LOSS*, the model converges the fastest and the convergence process is stable and smooth when the learning rate is between *0.0005* and *0.001*. Therefore, a learning rate in this interval is chosen.

After a suitable network model has been trained and hyperparameters have been recorded, anti-jamming predictions can be made for real satellite energy data. Benchmark comparison using models with the same input–output structure: GRU, BiLSTM, TCN, and Transformer. Table 2 show the RMSE, MAE, and MAPE of different modeling approaches at different rotational speeds for ten periods, 20 s, and 100 s, respectively. These results collectively demonstrate the accuracy of the modeling methods in the short-term and long-term. From the table, it is observed that both LSTM and GRU achieve best prediction accuracy in comparison, and can be applied to both short-term and long-term data. The performances of LSTM and GRU are very similar, with their results being practically indistinguishable. Furthermore, BiLSTM, TCN, and Transformer achieve good prediction accuracy, although it is not sufficiently high.

Therefore, in this experiment, the LSTM, GRU, BiLSTM, TCN and Transformer methods are can be utilized for roll attitude determination. However, higher prediction accuracy does not guarantee superior performance

RPS	Time period (s)	Metric	LSTM	BiLSTM	GRU	TCN	Transformer
2	5	RMSE	0.0668	0.0723	**0.0646**	0.0887	0.0829
		MAE	**0.0509**	0.0575	0.0514	0.0696	0.0654
		MAPE	0.2325	0.2319	**0.2218**	0.2526	0.306
	20	RMSE	0.0667	0.0726	**0.0655**	0.0965	0.0949
		MAE	**0.0516**	0.0577	0.0523	0.0715	0.0703
		MAPE	**0.2239**	0.2311	0.2333	0.2509	0.313
	100	RMSE	**0.0669**	0.0775	0.0672	0.105	0.1046
		MAE	**0.0517**	0.0616	0.0546	0.0758	0.0975
		MAPE	**0.2235**	0.2646	0.2344	0.2739	0.319
10	1	RMSE	0.0702	0.0889	**0.0653**	0.0817	0.0866
		MAE	0.0546	0.0703	**0.0511**	0.0642	0.0681
		MAPE	0.2111	0.3051	**0.1846**	0.2525	0.2627
	20	RMSE	0.0711	0.0861	**0.0644**	0.0891	0.0927
		MAE	0.056	0.0685	**0.0512**	0.064	0.0673
		MAPE	0.2196	0.2962	**0.1933**	0.2528	0.2699
	100	RMSE	0.0717	0.0883	**0.0659**	0.0952	0.961
		MAE	0.0562	0.0705	**0.0524**	0.0739	0.075
		MAPE	0.2178	0.0301	**0.2039**	0.2707	0.2741
20	0.5	RMSE	**0.0758**	0.1238	0.0862	0.1219	0.1207
		MAE	**0.0606**	0.1006	0.0674	0.1004	0.0999
		MAPE	**0.2135**	0.3893	0.2337	0.3801	0.3807
	20	RMSE	**0.0783**	0.09	0.0803	0.0893	0.0895
		MAE	0.0661	0.0704	**0.0658**	0.064	0.064
		MAPE	**0.2277**	0.2753	**0.2277**	0.2454	0.2466
	100	RMSE	**0.0782**	0.101	0.079	0.1014	0.095
		MAE	**0.0645**	0.0718	0.0649	0.0698	0.0677
		MAPE	0.2229	0.251	**0.221**	0.2456	0.2464

Table 2. The RMSE, MAE, and MAPE between the predicted and practice data (normalized to [0, 1]) of different methods in short-term and long-term periods. The bold ones denote the best performance on the corresponding metric.

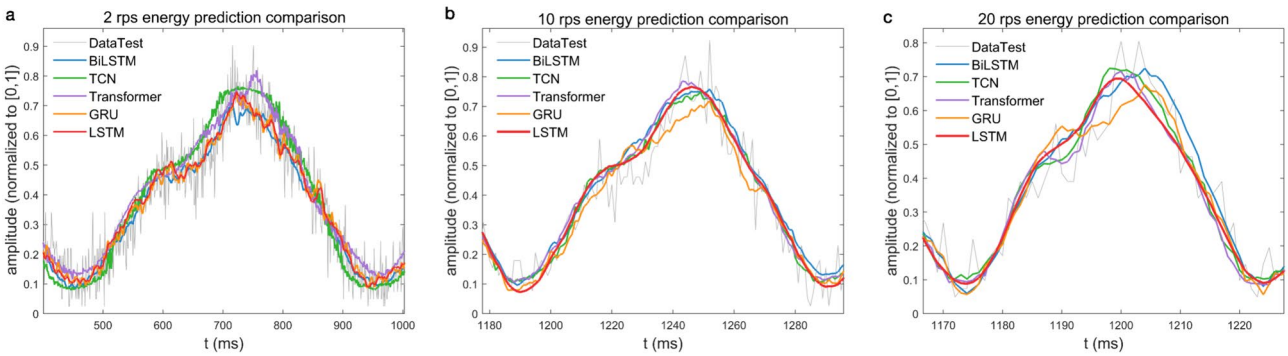

Fig. 15. Comparison of the original measured data with the predicted data using the LSTM, GRU, Transformer, TCN and BiLSTM method: (**a**) 2 rps. (**b**) 10 rps. (**c**) 20 rps.

in this study. As shown in Fig. 15, the prediction results are in line with the expected results when the model was trained. Overall, rotational speed is inversely proportional to energy density within a cycle. At lower rotational speeds, all methods exhibit slight fluctuations, with LSTM and GRU performing optimally. At higher speeds, the LSTM method yields the most stable results, while other models show varying degrees of instability. During peak energy intervals, where interference is most pronounced, GRU underperforms compared to LSTM in critical prediction phases. The LSTM method can not only adapt to the trend of the actual satellite energy but also predict stable and smooth energy after removing the jamming. The predicted satellite energy peaks have a single number and a stable relative position in one period, which is in line with the conditions set in this paper for utilizing satellite energy for attitude determination.

To investigate prediction accuracy in specific time intervals, uncertainty testing based on MC-Dropout[44] was conducted for both LSTM and GRU methods. Confidence intervals (CIs) of 50%, 95%, and 99% were derived from 100 sampling iterations. Results (Fig. 16) indicate higher uncertainty near energy peaks. The LSTM method exhibits narrower, smoother uncertainty ranges, whereas GRU shows broader and more variable ranges. Despite GRU's competitive accuracy, its practical performance is less reliable than LSTM under these conditions.

In this paper, six methods are used for comparison in the final test of the rolling attitude results of the vehicle. These methods include the traditional LS method, the LSTM method, the GRU method, the Transformer method, the TCN method and the BiLSTM method. In the LS method, it determines roll attitude based on the periodic changes identified in the originally observed energy of the five GEO satellites. For the test results, the roll angle data output from the Hall sensor in real time is used as a trusted reference value. First, the error between the roll angle solved by each method and the Hall roll angle is explored, as shown in Fig. 17. From the figures, it is easy to see that the jitter of the LSTM method is smaller than those of another methods for both low- and high-speed conditions. Next is Transformer and GRU, both of which have a similar level of LSTM. This finding provides proof that the LSTM method is more stable in solving the roll angle.

Table 3 lists the results of the roll angle determination for different rotational speeds under the LSTM, GRU, Transformer, TCN, BiLSTM and LS methods. In terms of the *StD*, the roll angle determined using the LSTM method exhibits less error compared to that of the other methods. On average, the LSTM method yields roll angles with less error at both low and high rotational speeds. Numerically, the degree of error is reduced by 48.97% points compared to that of the conventional LS method, outperforming BiLSTM, TCN, Transformer and GRU. In terms of the $RMSE_{Hall}$, the accuracy of the results is analyzed in terms of the roll angle output from the Hall sensor in real time. The accuracy of the roll angle solved by the LSTM method is significantly better than that of the LS method, with a numerical decrease of 48.20% with respect to the Hall real-time roll angle error, and this method can be applied to both high and low rotational speeds. These findings underscore LSTM's unique balance of memory retention and noise resilience, making it ideal for GNSS-based attitude determination in dynamic rotational environments. In summary, the roll angles of the vehicle measured by the LSTM method are substantially better than those measured by the LS and other methods in terms of stability and accuracy at different rotational speeds.

After completing the experimental analysis of the deep learning approach for roll attitude determination, this study further explored the integration of LSTM with the Extended Kalman Filter (EKF). The energy signals predicted by the LSTM were subsequently fed into the EKF for continued processing. Experiments reveal that integrating LSTM predictions with an EKF yields limited jitter reduction at low rotational speeds (2r/s), whereas significant improvement (~ 10°) is observed at higher speeds (10/20r/s) compared with only EKF. This discrepancy stems from insufficient noise resistance at low speeds. At 2r/s (period = 0.5 s), prolonged exposure to multipath interference and noise within each cycle amplifies localized prediction errors. While LSTM captures temporal patterns, its sensitivity to intermittent disturbances increases over long sequences. Moreover, EKF's motion model poorly matches the slow dynamics, failing to correct low-frequency LSTM errors. At 20r/s (period = 0.05 s), concentrated noise and pronounced periodicity allow LSTM to precisely track peak phases via short-term memory. Concurrently, EKF's dynamic model absorbs this enhancement, enabling complementary "LSTM coarse-tuning + EKF fine-adjustment."

Discussion

The free-space transmission Eq. (21) for the satellite signal power has been frequently mentioned in past research.

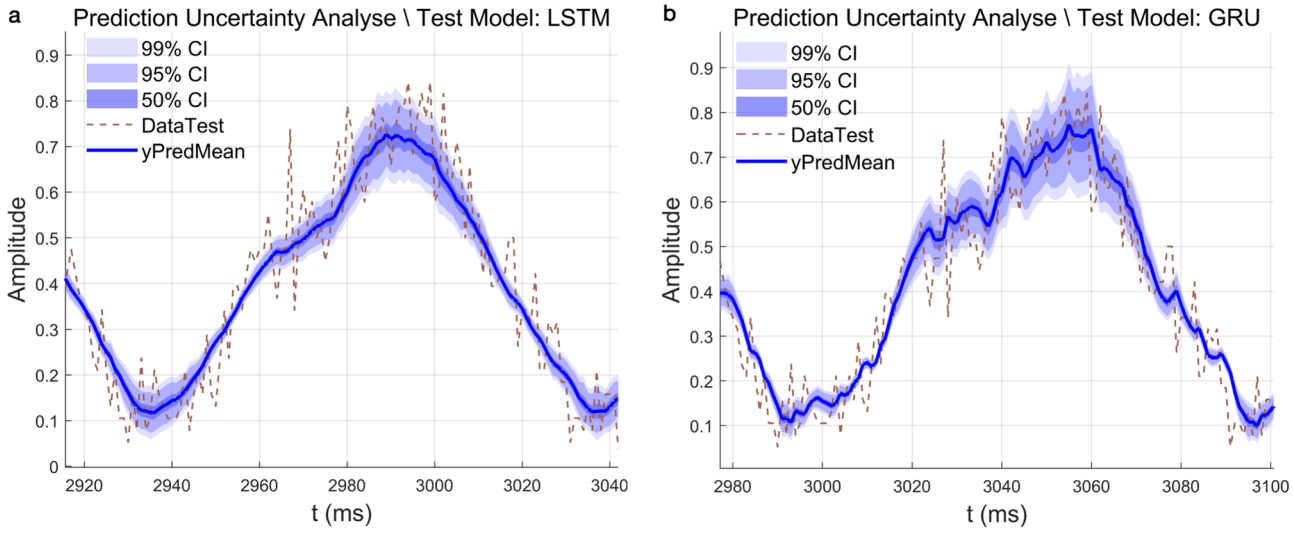

Fig. 16. Uncertainty estimates of predicted results at 10 rps: (**a**) LSTM model. (**b**) GRU model.

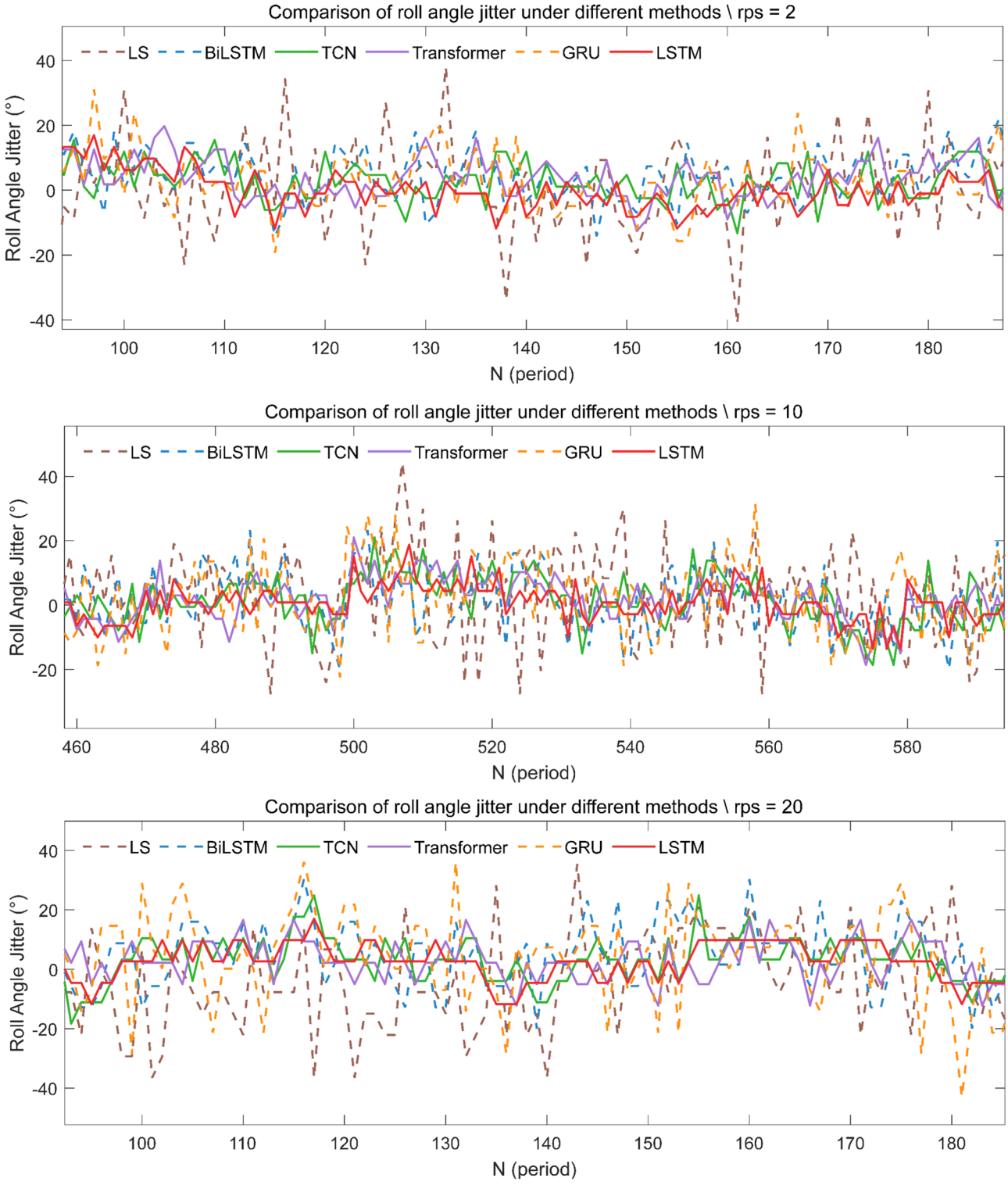

Fig. 17. Changes in the difference between the roll angle and Hall roll angle for each period solved using different methods.

Method	2r/s		10r/s		20r/s		Average	
	StD (°)	$RMSE_{Hall}$ (°)	*StD* (°)	$RMSE_{Hall}$ (°)	*StD* (°)	$RMSE_{Hall}$ (°)	StD (°)	$RMSE_{Hall}$ (°)
LS	11.69	12.97	14.68	15.08	15.83	15.89	14.07	14.65
BiLSTM	11.56	12.32	9.81	11.08	10.08	11.86	10.48	11.75
TCN	9.86	10.54	7.68	8.55	8.16	9.17	8.57	9.42
Transformer	9.59	10.13	7.28	7.90	7.88	8.39	8.25	8.81
GRU	10.32	11.36	10.55	12.20	10.26	12.01	10.38	11.86
LSTM	**8.13**	**8.50**	**6.86**	**7.25**	**6.55**	**7.01**	**7.18**	**7.59**

Table 3. StD for the roll angle solution results, and the $RMSE_{Hall}$ with respect to the Hall end for different methods and rotational speeds and every period. The bold ones denote the best performance on the corresponding metric.

$$\begin{aligned} P_r &= G_T + P_A \\ &= G_T + P_T + G_r + 20\lg\left(\frac{\lambda}{4\pi R}\right) \end{aligned} \tag{20}$$

where P_r represents the receiver antenna power; G_T represents the transmitting antenna gain; P_A represents the antenna surface signal power; P_T represents the transmitting power of the satellite signal; G_r represents the receiver antenna gain; λ represents the wavelength of the satellite carrier signal; and R represents the geometrical distance between the satellite and the receiving antenna.

The application of the real satellite energy can be further researched based on this equation. However, this research direction has not attracted much attention. The reason for this is mainly because of the limitations in the energy reception process that make it neglectable. In the research for this paper, these limitations are addressed by utilizing GEO satellite properties and LSTM methods. However, there are still issues to be considered. Since non-GEO satellites have a subsatellite point track distributed around the Earth, they undergo a certain regular motion with respect to the user on the ground. This will result in a shift in the angle of incidence of the non-GEO satellite signals, which will further affect the roll angle. In the satellite energy waveform, the change in the peak position will be represented, and by analyzing the peak index of each period, a fixed slope, i.e., regular changes in the index, can be found. Predicting the non-GEO satellite energy using a model trained on the GEO satellite energy will result in an inability to fully adapt to regular changes in peak position. Although training a model derived from retraining using a set of non-GEO satellite energies is beneficial for improving the prediction, there is no guarantee that it can be applied to all non-GEO satellites. This problem can be solved by training models with arbitrary non-GEO satellite energies separately, but this method becomes too complicated as the number of satellites increases. Subsequently, a more suitable training method or optimized model needs to be found to better adapt to this situation.

Second, the deep learning methods used in this paper perform well but have significant room for improvement. Uncertainty analysis shows they exhibit higher uncertainty during critical peak periods, greatly affecting roll attitude determination. Future research can enhance the fusion model and training strategies to improve prediction accuracy during these periods. Additionally, real-time prediction is a key factor. For example, while the Transformer model employed here is effective, it proved inefficient in real-time testing. Balancing prediction accuracy and efficiency is thus essential.

In conclusion, there is still much potential for the development of the application of satellite energy to vehicle attitude determination, whether it is the remediation of limitations, further optimization of the method, or subsequent in-depth processing.

Concluding remarks

The RMPA gain principle shows that the theoretically received satellite energy has a stable period and peak value, similar to that of a sine–cosine function. This property of the real-time roll attitude of flight vehicles can be solved by receiving satellite energy. By analyzing the properties of GEO satellites, it can be proven that the GEO satellite energy-changing rule and peak value characteristics are stable. When the GEO satellite signal energy is used for vehicle roll angle detection, empirical data can be used to improve the accuracy of roll angle measurements. In actual measurements, the satellite energy signal will inevitably appear in the process of sending and receiving noise jamming and multipath effects, resulting in unpredictable and different degrees of energy received by the RMPA. Research has shown that the introduction of the LSTM neural network deep learning method can effectively suppress this effect. The original properties of the energy, regardless of the duration, can be substantially restored by the method in this paper with strong generalizability and robustness. The experiments show that the roll angle self-error solved by using the LSTM method is reduced by 48.97% on average compared to the direct solving of the LS method, and the roll angle error is reduced by 48.20% on average compared to the determined roll angle error of the Hall sensor. It can be assumed that the method used is not affected by the test time, rotational speed, different GEO satellites, or the long or short term. Although the LS method can provide an effective solution for energy signal processing, it needs to obtain data from several satellites at the same time to achieve considerable results and is not suitable for processing in variable situations or real-time conditions. The roll attitude determination method based on the jamming energy of GEO satellites

and the LSTM neural network proposed in this paper provides new ideas and solutions for the field of attitude determination of rotation vehicles using GNSS.

Data availability

Example data is available at zenodo[45] (https://doi.org/10.5281/zenodo.15252235). More data will be made available on reasonable request from the corresponding author.

Code availability

All code used for data analysis is available at zenodo[45] (https://doi.org/10.5281/zenodo.15252235).

Received: 5 July 2024; Accepted: 5 May 2025
Published online: 23 May 2025

References

1. Dahiya, S., Saini, V. & Singh, A. K. GNSS signal processing based attitude determination of spinning projectiles. *IEEE Trans. Aerosp. Electron. Syst.* **58**, 4506–4516 (2022).
2. Titterton, D. & Weston, J. *Strapdown Inertial Navigation Technology*. (IET Digital Library, 2004). https://doi.org/10.1049/PBRA017E.
3. Lin, C.-F. *Modern Navigation Guidance and Control Processing* (Prentice Hall, 1991).
4. Doty, J. H. Advanced Spinning-Vehicle Navigation—A New Technique in Navigation of Munitions. in 745–754 (2001).
5. Qiu, Z., Qian, H. & Wang, G. Adaptive robust cubature Kalman filtering for satellite attitude estimation. *Chin. J. Aeronaut.* **31**, 806–819 (2018).
6. Shen, Q., Li, M. & Gong, R. GPS positioning algorithm for a spinning vehicle with discontinuous signals received by a single-patch antenna. *GPS Solut.* **21**, 1491–1502 (2017).
7. Larchenko, A. V. An attitude sensing device. *Instrum Exp. Tech.* **54**, 445–446 (2011).
8. Wang, J. et al. Performance in solar orientation determination for regular pyramid sun sensors. *Sensors* **19**, 1424 (2019).
9. Wilson, T., Angal, A. & Xiong, X. Orbital path and spacecraft attitude correction for the MODIS lunar spatial characterization. *IEEE Trans. Geosci. Remote Sensing* **58**, 1063–1073 (2020).
10. Park, S. K. & Suh, Y. S. A zero velocity detection algorithm using inertial sensors for pedestrian navigation systems. *Sensors* **10**, 9163–9178 (2010).
11. Singh, S., Bhattacharya, K., Ramaswamy, S. & Rao, C. Angular velocity-measurement using rate gyros in a spinning vehicle. *IEEE Trans. Aerosp. Electron. Syst.* **11**, 905–907 (1975).
12. Pei, C. Attitude determination algorithms for spinning satellites using single antenna GPS receiver and MEMS gyro. *Aerosp. Sci. Technol.* **26**, 10–15 (2013).
13. No, H., Cho, A. & Kee, C. Attitude estimation method for small UAV under accelerative environment. *GPS Solut.* **19**, 343–355 (2015).
14. Hou, B., He, Z., Zhou, H. & Wang, J. Integrated design and accuracy analysis of star sensor and gyro on the same benchmark for satellite attitude determination system. *IEEE/CAA J. Autom. Sinica* **6**, 1074–1080 (2019).
15. Pan, J. et al. Estimation and correction of azimuth and attitude errors of attitude tracking for vehicular spacecraft. *IEEE Trans. Instrum. Meas.* **72**, 1–10 (2023).
16. Lee, J. Y. et al. Adaptive GPS/INS integration for relative navigation. *GPS Solut.* **20**, 63–75 (2016).
17. Zhang, J. et al. Analysis and compensation of installation errors for rotating semi-strapdown inertial navigation system. *IEEE Access* **7**, 101019–101030 (2019).
18. Li, R., Wu, P., Feng, L., Tong, H. & Ren, Z. Assisted-GNSS positioning algorithm based on one-way fuzzy time information. *Heliyon* **9**, e20318 (2023).
19. Shu, Y. et al. High-rate attitude determination of moving vehicles with GNSS: GPS, BDS, GLONASS, and Galileo. *IEEE Trans. Instrum. Meas.* **71**, 1–13 (2022).
20. Mahato, S. et al. Visibility anomaly of GNSS satellite and support from regional systems. *Curr. Sci.* **119**, 1774–1782 (2020).
21. Hong, J.-H., Kim, Y.-J. & Ryoo, C.-K. Roll angle estimation for smart projectiles using a single patch antenna. *J. Guid. Control. Dyn.* **43**, 1772–1780 (2020).
22. Deng, Z., Shen, Q. & Deng, Z. Roll angle measurement for a spinning vehicle based on GPS signals received by a single-patch antenna. *Sensors* **18**, 3479 (2018).
23. Lee, H. S., Park, H., Kim, K., Lee, J. G. & Park, C. G. Roll angle estimation for smart munitions under GPS jamming environment. *IFAC Proc.* **41**, 9499–9504 (2008).
24. Tenn, H.-K., Jan, S.-S. & Hsiao, F.-B. Pitch and roll attitude estimation of a small-scaled helicopter using single antenna GPS with gyroscopes. *GPS Solut* **13**, 209–220 (2009).
25. Yang, C., Guo, J. & Zhao, Q. Yaw attitudes for BDS-3 IGSO and MEO satellites: Estimation, validation and modeling with intersatellite link observations. *J. Geod* **97**, 1–15 (2023).
26. Dai, X. et al. Estimating the yaw-attitude of BDS IGSO and MEO satellites. *J. Geodesy* **89**, 1005–1018 (2015).
27. Ma, X., Hu, Y. & Dong, X. Navigation accuracy and applicability analysis of GNSS technology in GEO and IGSO spacecraft. *GNSS World China* **47**, 1–8 (2022).
28. Guan, M., Xu, T., Li, M., Gao, F. & Mu, D. Navigation in GEO, HEO, and lunar trajectory using multi-GNSS sidelobe signals. *Remote Sens.* **14**, 318 (2022).
29. Graves, A. et al. Hybrid computing using a neural network with dynamic external memory. *Nature* **538**, 471–476 (2016).
30. Goodfellow, I., Bengio, Y. & Courville, A. *Deep Learning* (MIT Press, 2016).
31. Guo, M. et al. Research on time series prediction of the flow field in supersonic combustor based on deep learning. *Aerosp. Sci. Technol.* **140**, 108459 (2023).
32. Hochreiter, S. & Schmidhuber, J. Long short-term memory. *Neural Comput.* **9**, 1735–1780 (1997).
33. Liu, Y. et al. Detection and mitigation of time synchronization attacks based on long short-term memory neural network. *GPS Solut.* **28**, 46 (2023).
34. Cho, K. *et al.* Learning Phrase Representations using RNN Encoder-Decoder for Statistical Machine Translation. https://doi.org/10.48550/arXiv.1406.1078 (2014).
35. Graves, A. & Schmidhuber, J. Framewise phoneme classification with bidirectional LSTM networks. In *Proceedings. 2005 IEEE International Joint Conference on Neural Networks, 2005.* vol. 4 2047–2052 (2005).
36. Bai, S., Kolter, J. Z. & Koltun, V. An empirical evaluation of generic convolutional and recurrent networks for sequence modeling. https://doi.org/10.48550/arXiv.1803.01271 (2018).
37. Vaswani, A. *et al.* Attention is all you need. https://doi.org/10.48550/arXiv.1706.03762 (2023).

38. Luo, Y., Wang, Y., Wu, S. & Wang, P. Multipath effects on vector tracking algorithm for GNSS signal. *Sci. China Inf. Sci.* **57**, 1–13 (2014).
39. Candan, Ç. & Inan, H. A unified framework for derivation and implementation of Savitzky-Golay filters. *Signal Process.* **104**, 203–211 (2014).
40. Srivastava, N., Hinton, G., Krizhevsky, A., Sutskever, I. & Salakhutdinov, R. Dropout: A simple way to prevent neural networks from overfitting. *J. Mach. Learn. Res.* **15**, 1929–1958 (2014).
41. Du, S. S., Zhai, X., Poczos, B. & Singh, A. Gradient descent provably optimizes over-parameterized neural networks. https://arxiv.org/abs/1810.02054v2 (2018).
42. Du, S. S., Lee, J. D., Li, H., Wang, L. & Zhai, X. Gradient descent finds global minima of deep neural networks. https://doi.org/10.48550/arXiv.1811.03804 (2019).
43. Arora, S., Cohen, N., Golowich, N. & Hu, W. A convergence analysis of gradient descent for deep linear neural networks. https://doi.org/10.48550/arXiv.1810.02281 (2019).
44. Gal, Y. & Ghahramani, Z. Dropout as a Bayesian approximation: Representing model uncertainty in deep learning. https://doi.org/10.48550/arXiv.1506.02142 (2016).
45. Li, R. Code and example data for 'A Roll Attitude Determination Method Based on the Jamming Energy of GEO Satellites and an LSTM Neural Network.' Zenodo https://doi.org/10.5281/zenodo.15252235 (2025).

Acknowledgements

This paper was supported by Key research and development projects of Hunan Provincial Department of science and technology in 2022 (Grant No. 2022GK2026), Hunan Natural Science Foundation Project (Grant No. 2022JJ30636), Excellent Youth Program of the Scientific Research Program of the Department of Education of Hunan Province (Grant No. 22B0838), Science and technology plan project of Hunan Provincial Department of Natural Resources (Grant No. 2023-78), Aid program for Science and Technology Innovative Research Team in Higher Educational Institutions of Hunan Province, Open Fund of Xi'an Key Laboratory of Integrated Transport Big data and Intelligent Control (Chang'an University) (Grant No. 300102343515), Key program of Hunan Provincial Department of science and technology support (Grant No. 23A0609), Key research and development projects of Hunan Provincial Department of science and technology(Grant No. 2024JK2062), Hunan Natural Science Foundation Project (Grant No. 2024JJ9190), and National Key Laboratory of Unmanned Aerial Vehicle Technology in NPU (Grant No. WR202403).

Author contributions

RL, LF, and PW contributed to the study conception and design. RL designed and performed the experiment, provided part of the methodology, and wrote the paper. LF conducted project management and provided the analysis of methodology. PW presented the basic idea of the paper and provided comments on the manuscript. XD and HS acquired and managed data. All authors have read and agreed to the published version of the manuscript.

Declarations

Competing interests

The authors declare no competing interests.

Ethical approval and consent to participate

Not applicable.

Additional information

Correspondence and requests for materials should be addressed to L.F.